



## Regional dynamical and statistical downscaling temperature, humidity and windspeed for the Beijing region under stratospheric aerosol injection geoengineering

Jun Wang<sup>1</sup>, John C. Moore<sup>1,2\*</sup>, Liyun Zhao<sup>1\*</sup>, Chao Yue<sup>1</sup>, Zhenhua Di<sup>3</sup>

<sup>1</sup>College of Global Change and Earth Systems Science, Beijing Normal University, Beijing, China

5 <sup>2</sup>Arctic Center, University of Lapland, Rovaniemi, Finland

<sup>3</sup>State Key Laboratory of Earth Surface Processes and Resource Ecology, Faculty of Geographical Science, Beijing Normal University, Beijing 100875, China

*Correspondence to:* zhaoliyun@bnu.edu.cn, john.moore.bnu@gmail.com

**Abstract.** We use four Earth System Model (ESM) to simulate climate under the modest greenhouse emissions RCP4.5, the “business-as-usual” RCP8.5 and the stratospheric aerosol injection G4 geoengineering scenarios. These drive a 10 km resolution dynamically downscaled model (WRF), and a statistically bias corrected (ISIMIP) and downscaled simulation in a 450×330 km domain containing the Beijing province, ranging from 2000 m elevations to sea level. The 1980s simulations of surface temperatures, humidities and windspeeds using statistical bias correction makes for a better estimate of mean climate determined by ERA5 reanalysis data than does the WRF simulation. However correcting WRF output with Quantile-Delta Mapping bias correction removes the offsets in mean state and results in WRF better reproducing observations over 2007-2017 than ISIMIP bias correction. WRF simulations show consistently 0.5°C higher mean annual temperatures than from ISIMIP due both to the better resolved city centers and also to warmer winter temperatures. In the 2060s WRF produces consistently larger spatial ranges of surface temperatures, humidities and windspeeds than ISIMIP downscaling across the three future scenarios. WRF and ISIMIP methods produce very similar spatial patterns of temperature with G4 are always cooler than RCP4.5 and RCP8.5, by a slightly larger amount with ISIMIP than WRF. Humidity scenario differences vary greatly between ESM and hence ISIMIP downscaling, while for WRF the results are far more consistent across ESM and show only small changes between scenarios. Mean windspeeds show similarly small changes over the domain, although G4 is significantly windier under WRF than either RCP scenario.

10  
15  
20  
25



## 1 Introduction

The global-mean surface air temperature has increased by 0.9°C-1.2°C relative to 1850-1900 (Eyring et al., 2021), with a rapid rise during the 2010s. Extreme climate events are becoming more frequent  
30 (Pachauri et al., 2014), impacting human health and mortality rates (Pielke et al., 2013). ESM despite global in extent, cannot simulate phenomena smaller than their spatial resolution (typically 1-2°) with the same fidelity as higher resolution models with much smaller domains. Higher resolution models include regional climate models and the Weather Research and Forecasting model (WRF) which are generally driven by ESMs at their lateral boundaries. WRF has been widely used as a dynamical  
35 downscaling method for future climate projection at small and regional scales (Bao et al., 2015; Brewer and Mass et al, 2016; Kong et al., 2019). Kong et al. (2019) found that WRF was satisfactory in reproducing spatiotemporal distribution and trends of extreme climate indices for China.

Geoengineering via increasing planetary albedo as a method of avoiding the worst excesses of climate  
40 heating has been actively discussed in climate research for well over a decade (Shepherd, 2009). The most widely studied albedo modification type (e.g. Lenton et al., 2009; Robock et al., 2009) is via stratospheric aerosol injection (SAI). To standardize and aid the evaluation of SAI in ESM simulations, Kravitz et al. (2011) proposed the Geoengineering Model Intercomparison Project (GeoMIP), with Phase 1 including two different SAI scenarios using sulfates as the aerosol, and with greenhouse gas  
45 emissions from the Representative Concentration Pathway (RCP) 4.5 scenario. The impacts of SAI on temperature (Schmidt et al., 2012), precipitation (Tilmes et al., 2013), and the cryosphere (Moore et al., 2019) show that indeed the global mean temperatures are reduced, albeit with imperfections such as relative over-cooling of the tropics and under-cooling of the polar regions, and with relatively modest impacts on precipitation, especially compared with the less mitigated greenhouse gas scenarios. Several  
50 studies have considered global-scale impacts on temperature and precipitation extremes under both SAI and other geoengineering types designed to enhance planetary albedo (Curry et al., 2014; Aswathy et al., 2015; Ji et al., 2018), and some studies have focused on regional impacts such as in Europe (Jones et al., 2018), East Asia (Kim et al., 2020), or the Maritime Continent (Kuswanto et al., 2021).

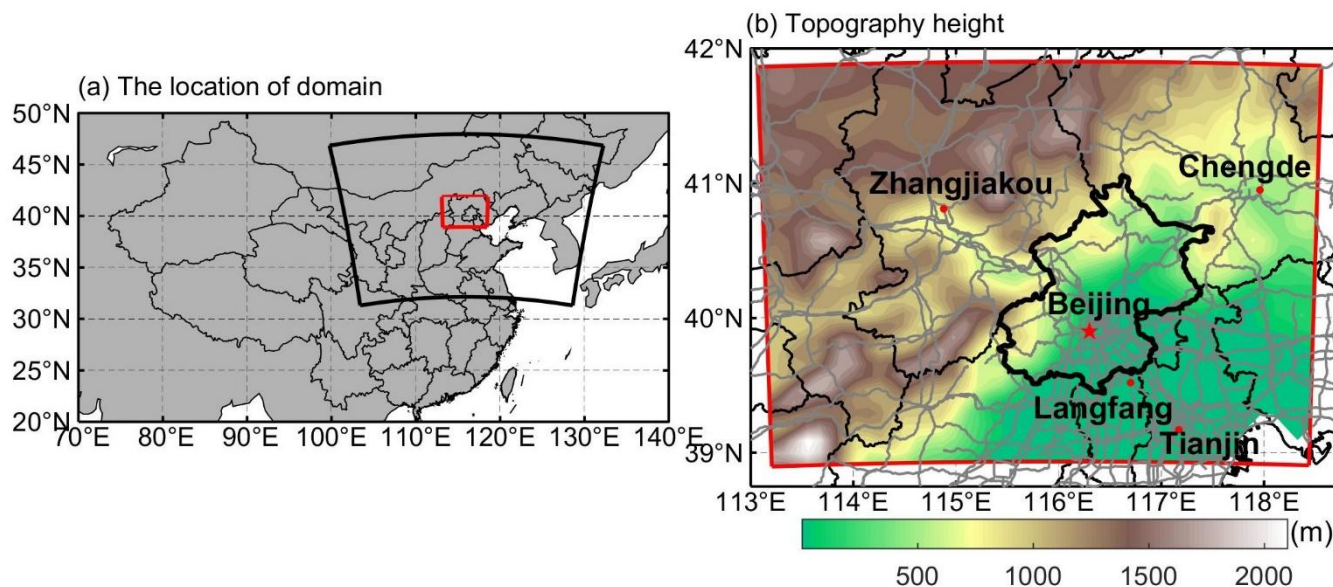


55 Statistical downscaling has often been used as an alternative to dynamical methods, avoiding the  
significant computing resources needed to run models such as WRF. Statistical downscaling is based on  
the relationships found historically between ESM output and observed climate variables and is very  
widely used in regional impact studies (Wilby et al., 2004). All models produce results with a bias from  
observations, and future simulations require either bias correction, or results are shown as climate  
60 anomalies relative to some control scenario. The ISIMIP (<https://www.isimip.org/>) consortium has  
produced methods (Hempel et al., 2013) widely used to correct the bias from CMIP5 (Climate Model  
Intercomparison Project phase 5) and GeoMIP outputs (McSweeney et al., 2016; Moore et al., 2019;  
Kuswanto et al., 2021). In our paper, we compare ISIMIP statistical downscaling methods and output  
from WRF dynamical downscaling and assess their performance for simulating the climate condition in  
65 the provinces around Beijing under SAI.

The greater Beijing region lies in complex terrain, surrounded by hills and mountains on three sides,  
with a flat plain to the southeast coast (Fig. 1). We explore the effect of geoengineering on surface  
temperature, wind and humidity in this domain. We nest a 10 km resolution domain inside a much  
70 larger 30 km resolution domain, driven at the boundaries with ESM output. We use the WRF model to  
dynamically downscale three time slices: 1979-1989, 2007-2017 and 2059-2069 driven by four ESM  
simulating the Historical, RCP 4.5, RCP8.5, and the GeoMIP G4 scenarios (Table 1). The 10 km  
resolution we use is not designed to study urban processes. Instead, we examine differences in  
downscaling at resolutions higher than, but comparable with, statistical downscaling methods that are  
75 likely to continue to be used in most geoengineering studies globally. To the best of our knowledge, this  
paper is the first to make dynamic downscaling of geoengineering scenarios.

**Table 1.** The simulations in our study.

Periods	Scenarios	Goal of the simulation
1979-1989	Historical	Compare ISIMIP statistical downscaling and bias-correction with WRF
2007-2017	RCP4.5	Assess the performance of ISIMIP and WRF with bias-correction
2059-2069	RCP4.5, RCP8.5, G4	Future downscaled climates by ISIMIP and WRF with bias-correction



80

**Figure 1.** (a) Map of East Asia with Chinese provincial boundaries marked in black. The 10 km WRF domain (red box) is nested inside the 30 km resolution domain (large black sector), which is centered on 116°E, 40°N on a Lambert projection. (b) The topography and primary roads (gray curves) of the 10 km resolution domain from panel (a). The provincial boundaries are marked in black with the heavier line demarking the Beijing province. The major metropolitan centers of Beijing, Tianjin, Chengde and Langfang are marked in red.

85

We firstly show the differences between statistical downscaling with bias correction and dynamical downscaling without bias correction in the 1979-1989 period. This will show that statistical downscaled and bias corrected result, by design, has closer agreement with observations, despite its absence of physics, than the dynamically downscaled simulation. For the recent past period 2007-2017 we use the quantile delta mapping method to statistically correct the bias of WRF simulation and assess its performance. Finally, we show the projections in the future period 2059-2069 for the greater Beijing region where global temperature differences under different greenhouse gas and G4 scenarios are known to be large. The paper is organized as follows: Section 2 describes the WRF model setup and parameterization, statistical downscaling and bias correction methods. The results from the historical simulation and future projections on the surface temperature, humidity, and wind speed are all given in Section 3. Finally, a summary of the main findings and conclusion is given in Section 4.

90

95



## 2 Data and Method

### 100 2.1 ESMs and Scenarios (Data Description)

We focus on exploring the effect of SAI on surface meteorological conditions (temperature, humidity, and wind) over the domain using four different dynamically and statistically downscaled ESMs. In the simulations, we use three different scenarios: RCP4.5 and RCP8.5 and the GeoMIP G4 scenario. RCP4.5 is a scenario that never exceeds a radiative forcing of  $4.5 \text{ W m}^{-2}$  (Thomson et al., 2011), while  
105 RCP8.5 is an unmitigated emissions scenario leading to a radiative forcing of  $8.5 \text{ W m}^{-2}$  at the end of the 21<sup>st</sup> century (Riahi et al., 2011). The GeoMIP experiment G4 specifies injection of sulfur dioxide into the equatorial lower stratosphere at a rate of 5 Mt per year from 2020 to 2069 (Kravitz et al., 2011). These scenarios span a useful range of climate scenarios: RCP4.5 is similar (Vandyck et al., 2016) to the expected trajectory of emissions under the 2015 Paris Climate Accord Nationally Determined  
110 Contributions (NDCs); RCP8.5 represents a formerly business-as-usual scenario that still provides a large signal to noise ratio “worst case” scenario; G4 represents a similar radiative forcing as a quarter of the 1991 Mount Pinatubo volcanic eruption every year. If SAI were ever done then it would certainly use a much more sophisticated injection procedure than G4, perhaps designed to maintain hemispheric temperature balance and preserve pole-equator temperature gradients (Macmartin and Kravitz, 2016).  
115 However, G4 levels of SAI are within the linear response of temperature reduction to material injected, and within a range of radiative forcing that might be plausible or reasonable to consider (Niemeier and Timmreck, 2015). GeoMIP has also developed new experiments for use with CMIP6 level ESMs (Kravitz et al., 2015).

120 ESM data required as input data for WRF includes meteorological fields, land surface and soil properties: specific humidity, air temperature, eastward wind, northward wind, near surface air pressure and the elevations of 30 pressure levels from 1000 hPa to 30 hPa, soil temperatures, humidities and water contents and sea level pressures. Only four ESMs can meet the data requirements (Table 2). We only use one single realization (r1i1p1 using the CMIP5 nomenclature) for each model since all  
125 downscaling runs are extremely computationally expensive and some of the models have only a single realization available.



**Table 2.** ESMs used in this study.

Model	Resolution (lon × lat)	Reference
BNU-ESM	128 × 64	Ji et al. (2014)
HadGEM2-ES	192 × 144	Collins et al. (2011)
MIROC-ESM	128 × 64	Watanabe et al. (2011)
MIROC-CHEM-ESM	128 × 64	Watanabe et al. (2011)

We also use the 31 km resolution ERA5 6-hourly reanalysis data during 1979/01/01-1989/12/31 to  
130 correct ESM climate fields at the domain boundaries as required by WRF (Hersbach et al., 2018). ERA5  
reanalysis near surface meteorological elements (2 m temperature, 2 m humidity and 10 m wind speed)  
are significantly correlated with observations over the area (Meng et al., 2018). We use daily  
temperature, humidity and wind from ERA5 for the period 1980-1989 and 2008-2017 to statistically  
bias correct the ESMs variables and assess the performance of WRF downscaling.

## 135 2.2 WRF

The WRF model adopts a compressible non-hydrostatic equilibrium equation, and a variety of physical  
parameterization schemes and data assimilation which can realize high-resolution weather forecasts at  
various scales (Michalakes et al., 2001). Xu et al. (2012) used WRF to improve the bias in a global  
climate model simulations of extreme weather events. WRF needs 6 hourly input data, which does not  
140 exist for most variables in the ESMs climate simulation output. So, we use the available monthly ESM  
data to estimate 6-hourly input data with a pseudo global warming downscaling method (PGW-DS,  
Kawase et al., 2009) using ERA5 data bilinearly interpolated to the same grid as the ESM output:

$$M_f = R_h - \overline{M}_h + \overline{M}_f \quad (1)$$

where  $M_f$  is the ESM-driven WRF model 6-hourly input data,  $R_h$  is 6-hourly data from ERA5  
145 reanalysis during the historical period, 1979-1989. For the period 1979-1989,  $\overline{M}_h$  is the monthly data of  
ERA5,  $\overline{M}_f$  is the monthly data of ESMs under historical scenario. For the period 2007-2017,  $\overline{M}_h$  is the  
monthly data of ESMs during 1979-1989 under historical scenario, and  $\overline{M}_f$  takes the monthly data of  
ESMs during 2007-2017 under RCP4.5. For the period 2059-2069,  $\overline{M}_h$  is the monthly data of ESMs  
during 1979-1989 under historical scenario, and  $\overline{M}_f$  takes the monthly data of ESMs during 2059-2069  
150 under RCP4.5, RCP8.5 and G4 scenarios.



This study uses WRF version 3.9.1 with 2 nested domains, where the inner domain (longitude  $\times$  latitude: 45 $\times$ 33) has a resolution of 10 km and the outer domain (80 $\times$ 58) has a resolution of 30 km (Fig. 1). The model has 30 vertical layers from the surface to 50 hPa. The integration timestep is 3 minutes. We set  
155 the parameterizations following a study on the numerical simulation of urbanization on regional climate in China (Wang et al., 2012) as follows: the WRF Single Moment 6-class (WSM6, Hong et al. 2006), the new version of rapid radiative transfer model (RRTMG, Iacono et al., 2008) for both the long-wave and short-wave radiation, the MM5 similarity surface layer scheme (Paulson et al, 1970), the Yonsei University (YSU) planetary boundary layer (PBL) scheme (Noh et al., 2003), the Kain-Fritsch scheme  
160 for atmospheric convection (Kain, 2004), and the Noah land surface model (Chen and Dudhia, 2001). Putting the ESMS data as initial and boundary conditions into the WRF Preprocessing System (WPS; Fig. 2) is challenging. We downloaded all the required monthly data (See Table S1) from 4 ESMS in the 3 periods (1979-1989, 2007-2017, 2059-2069) and 6-hourly historical data from ERA5 (1979-1989). Then, we used the PGW method to get the 6-hourly input data during three periods (see Equation 1).  
165 We then used Climate Data Operators (CDO) to convert the input data in NC format files into GRIB format files that WPS can recognize. In all three simulated periods, the initial year is considered as spin-up time and is not included in our analysis.

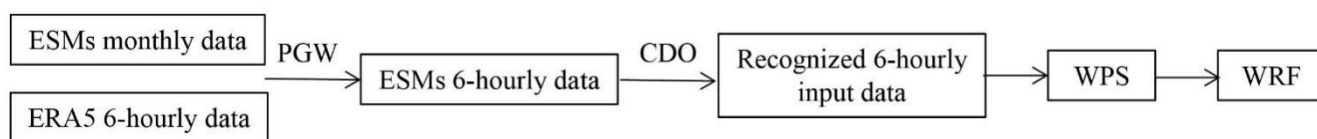


**Figure 2.** The WRF flow chart. PGW refers to the pseudo global warming downscaling method, and  
170 CDO refers to Climate Data Operators used for generating the WRF recognizable “GRIB” format input data. WPS is the WRF Preprocessing System.

### 2.3 ISIMIP statistical downscaling and bias correction

This method corrects daily variability on the premise that the monthly trend of the modeled variable is  
175 unchanged (Hempel et al., 2013) and includes two steps:



Step 1: Monthly bias corrected data is found by annual average difference between the model output and reanalysis data.

Step 2: Bias corrected daily data can be calculated by adding a linear regression residual:

$$M_d^* = (\overline{R_m} - \overline{M_m}) + M_m + \overline{B} \times (M_d - M_m). \quad (2)$$

180  $M_d^*$  is the bias corrected daily data.  $\overline{R_m}$  and  $\overline{M_m}$  are multi-year averaged values in one specific month from reanalysis data and model data, respectively.  $M_m$  and  $M_d$  are the monthly and daily model output in the specific month. The subscripts  $m$  and  $d$  represent monthly and daily, respectively.  $\overline{B}$  is the linear regression coefficient of daily residual values between observed data and model data. Here, we use the ERA5 reanalysis data as observed data in our study. For convenience we use the term ISIMIP-ESM to  
185 denote the output from the ESMs after applying the ISIMIP statistical downscaling and bias correction methodology.

## 2.4 Quantile Mapping (QM) and Quantile delta Mapping (QDM)

Quantile mapping has been widely used as a statistical bias-correction and downscaling method (Li and  
190 Babovic, 2019; Kuswanto et al., 2021), and annual and monthly biases of all variables can be reduced to nearly zero (Wilcke et al., 2013). As a bias correction method, quantile mapping can reproduce the frequency of different types of extreme heat wave events well (Schoof et al., 2019). Here we use the empirical CDF to correct the biases:

$$M_d^* = F_R^{-1}(F_H(M_d)). \quad (3)$$

195  $M_d^*$  is the daily data after bias correction,  $F$  is the cumulative distribution function (CDF) and  $F^{-1}$  is the inverse, subscript  $R$  represents the ERA5 reanalysis data, subscript  $H$  represents historical simulation results, and  $M_d$  is daily model output in the historical simulations. This method keeps the model and observational data CDFs as consistent as possible.

200 QDM is similar to QM but is non-stationary. It considers the time variability between the historical simulation and future projection, hence it is preferable for our task here (Salvi et al., 2011).

$$M_d^* = F_R^{-1}(F_F(M_d)) + (M_d - F_H^{-1}(F_F(M_d))). \quad (4)$$





The  $M_d^*$  and  $M_d$  are bias corrected and raw daily model output in the future simulations. The subscript  $R$  represents the ERA5 reanalysis data, the subscript  $F$  and  $H$  represents model outputs from future and  
205 historical simulations, respectively. To preserve the spatial information of the high resolution WRF model result, we do bias correction on daily value averaged in the whole inner domain (Fig. 1b) rather than separately for each grid point.

For the WRF simulations during 2007-2017 and 2059-2069, we use the QDM method to correct biases.  
210 Similar to ISIMIP-ESM, we use the terms WRF-ESM and WRF-QDM-ESM to represent results of WRF driven by the ESM and WRF driven by ESM after QDM bias correction, respectively.

### 3 Results

#### 3.1 Historical simulation: WRF and ISIMIP downscaling comparison

We compare the simulations of mean temperature, relative humidity, and wind speed from raw ESM  
215 output downscaled to ERA5 resolution, ISIMIP-ESM and WRF-ESM in Beijing during the 1980s in Fig. 3. Fig. 3a shows the annually averaged 2 m ERA5 temperatures in Beijing, with a mean of 7 °C and highs in the southeast (12 °C) and lows in the northwest, which correlates with the topography (Fig. 1). Relative humidity (Fig. 3e) varies between 50%-55%, with the city center a little drier than the suburbs. Similarly, wind speed is low in the city center with highs in the higher north-western hills and south-  
220 eastern plain (Fig. 3i).

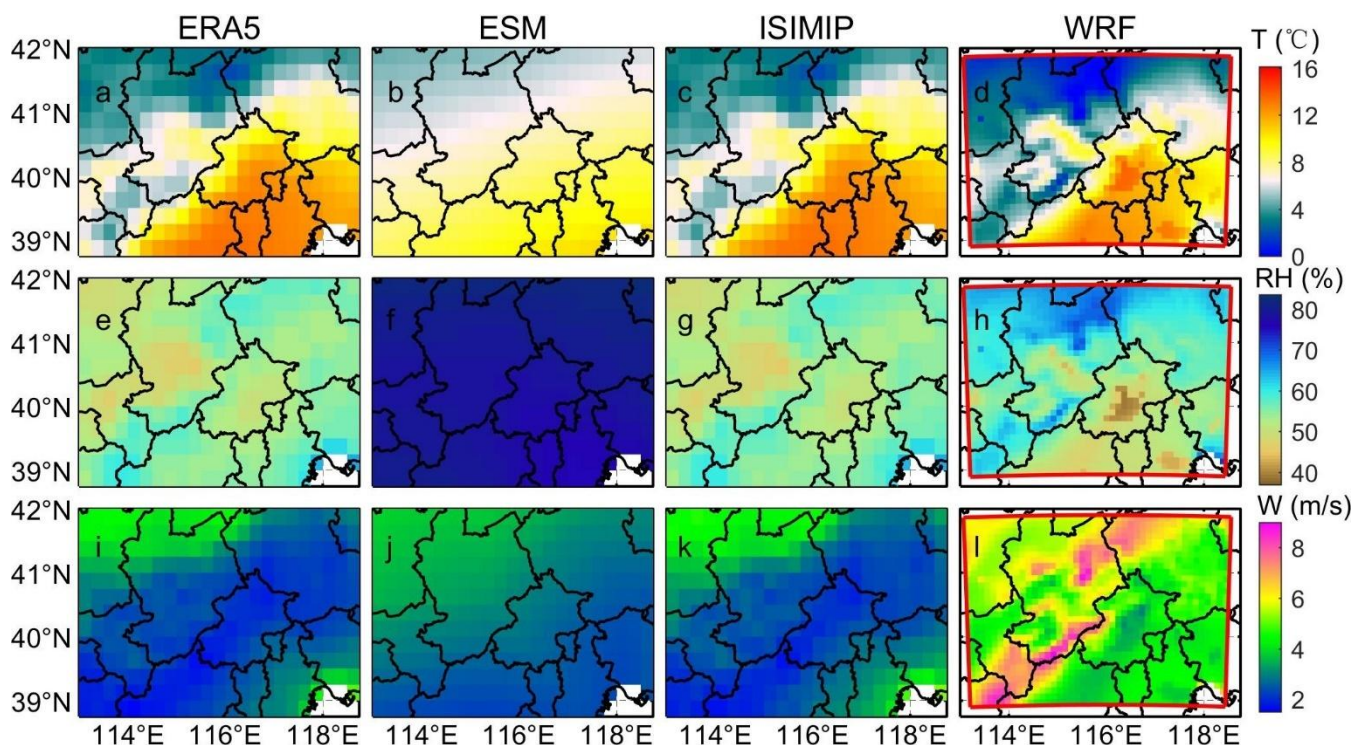


**Figure 3.** The region containing the high resolution WRF domain (red boundary in right column maps), with city boundaries marked in black. The spatial distribution of mean 2 m temperature (a-d), relative humidity (e-h) and 10 m wind speed (i-l) from ERA5, downscaled ESM ensemble mean before any bias correction, ISIMIP-ESM multi-ensemble mean and the WRF-ESM multi-ensemble mean in the high-resolution domain (Fig. 1) during 1980-1989. The results for the four ESM are shown separately in Figs. S1-S3 along with the bias corrected versions.

The temperatures from the raw ESM outputs in Beijing have less range than both ISIMIP-ESM and WRF-ESM results due to their coarser resolution, and obvious bias. The mean temperatures of MIROC-ESM and MIROC-ESM-CHEM over the domain are about 8°C while HadGEM2-ES and BNU-ESM are cooler, and all ESM have a large cold bias compared with ERA5 (Fig. S1). ISIMIP-ESM forces the model mean data to agree with ERA5 mean observations by design, and also downscales the ESM data to the observational resolution (Fig. 3c, 3g, 3k). The resulting ISIMIP-ESM means are indistinguishable by eye from the ERA5 mean in Fig. 3, though the ESM trends over time are preserved and the seasonality and other measures of variability are ESM-dependent and differ from ERA5.



WRF has a finer resolution than ERA5 and clearly shows higher temperatures in the center of Beijing with cool temperatures over the mountains. WRF temperatures driven by MIROC-ESM and MIROC-ESM-CHEM are higher in the Beijing and Tianjin city centers than ERA5, ISIMIP-MIROC and ISIMIP-MIROC-CHEM outputs, while the temperatures in the suburbs is a little lower than from ERA5  
240 and ISIMIP-ESM. Temperatures from HadGEM2-ES driven WRF are a little colder than that of ERA5 and ISIMIP-HadGEM2 over Beijing (Fig. S1). WRF also produces lower relative humidity in the center of Beijing and higher humidity in the north and west of city, consistent with the pattern of temperatures. Humidity under WRF tends to be lower in the urban center (45%) and higher in the suburban areas (60%) than ISIMIP and ERA5. Relative humidities of all ESM are higher than ERA5 (Fig. S2). The  
245 humidity of WRF under different ESMs is noticeably different from each other, although MIROC-ESM and MIROC-ESM-CHEM are similar (Fig. S2). Wind speeds in all ESMs are greater than ERA5, except HadGEM2-ES (Fig. S3). ISIMIP reduces all ESM to essentially the ERA5 pattern as with temperature and humidity. WRF winds for all four ESM are greatly overestimated. All WRF simulations have spatial patterns very different from ERA5, with maximums associated with the  
250 northern and western higher ground.

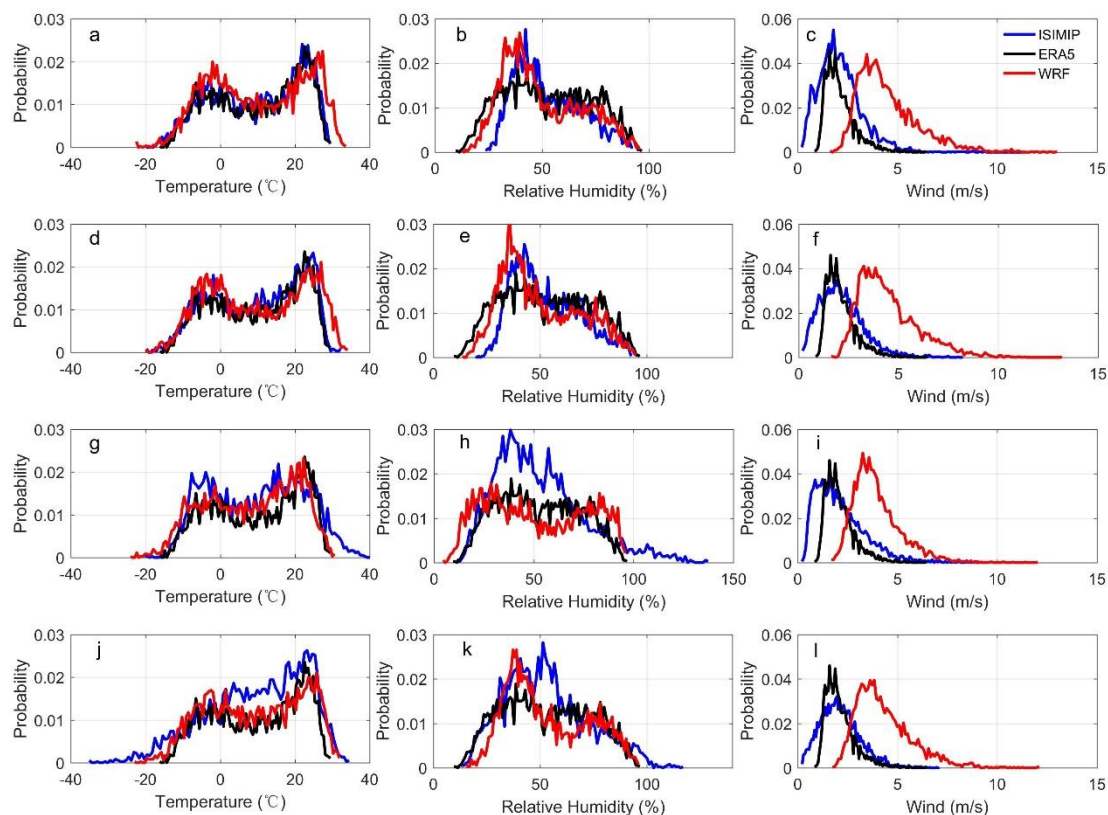
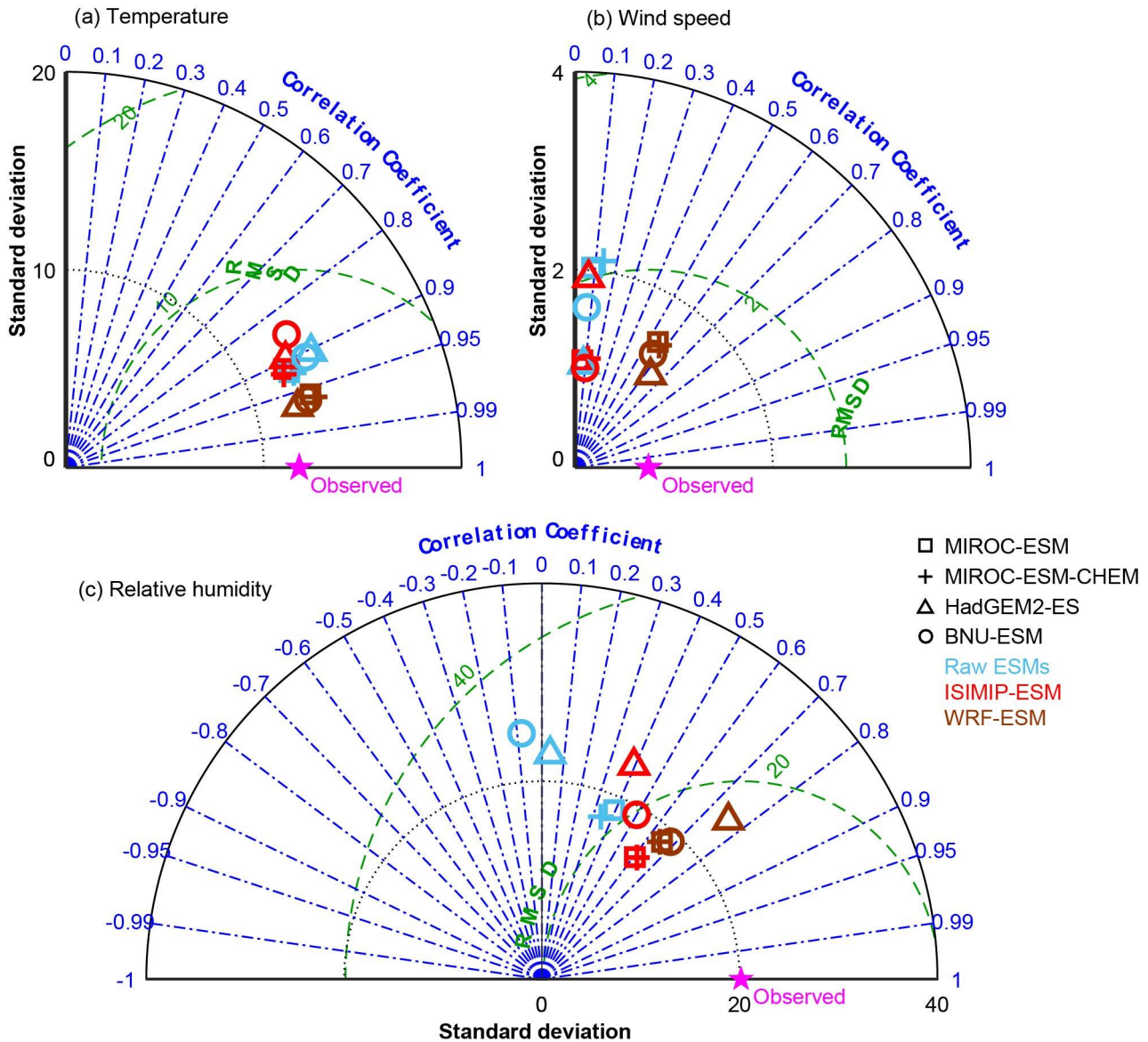


**Figure 4.** The probability density function (pdf) for daily mean temperature, relative humidity and wind speed for MIROC-ESM (a-c), MIROC-ESM-CHEM (d-f), HadGEM2-ES (g-i) and BNU-ESM (j-l) under WRF (red lines) and ISIMIP statistical bias correction method (blue lines) in the Beijing province (Fig. 1) during 1980-1989. The black line is ERA5 reanalysis data.

The temperature, relative humidity and windspeed distributions (Fig. 4) illustrate bias and across-ESM differences for the WRF simulations. Both MIROC-ESM and MIROC-ESM-CHEM overestimate the probability of high temperatures. ISIMIP-HadGEM2 overestimates likelihood of high temperatures compared with ERA5, while ISIMIP-BNU overestimates both high and low temperatures extremes. WRF performs well for all four ESM compared with ISIMIP which produces unphysical relative humidities exceeding 100% for HadGEM2-ES and BNU-ESM. ISIMIP winds for all four ESMs tend to increase the frequency of low winds and winds exceeding 5 m/s. WRF winds are close to twice that of ERA5. Overall, results after ISIMIP shows closer mean values to ERA5 while the pdfs for WRF are closer to ERA5, but the differences between ISIMIP and WRF are small except for wind speed.



265

270

**Figure 5.** Taylor diagram for daily temperature (a), wind speed (b) and relative humidity (c) of four ESMs using two downscaling methods, i.e., ISIMIP (red) and WRF (brown) compared to ERA5 data during 1980-1989 in Beijing. The blue symbols are the data from raw ESMs. The skill of downscaling methods is reflected by the distance from each symbol to the point labelled “ERA5”, the ERA5 reanalysis data. The blue lines are correlation coefficient which represents the similarity between each downscaling data and reanalysis data. The green contours are root mean standard deviation (RMSD), and black contours are standard deviation.



Fig. 5 shows the Taylor diagrams (Taylor, 2001), which can be used to assess the skill of two  
downscaling methods applied to meteorological data. Temperatures from raw MIROC-ESM and  
275 MIROC-ESM-CHEM output show better performance than the other two models. WRF has better  
correlation coefficient ( $>0.95$ ) than ISIMIP, and smaller RMSD for all four ESMS. Wind speed of all  
four ESMS outputs have correlation coefficients  $<0.1$  with ERA5. ISIMIP greatly reduces errors and  
variance but does not improve correlation. WRF has the better correlation, lower errors and shows  
better skill on simulating the wind speed than ISIMIP, despite its systematic bias in magnitude.

### 280 3.2 Bias correction for WRF

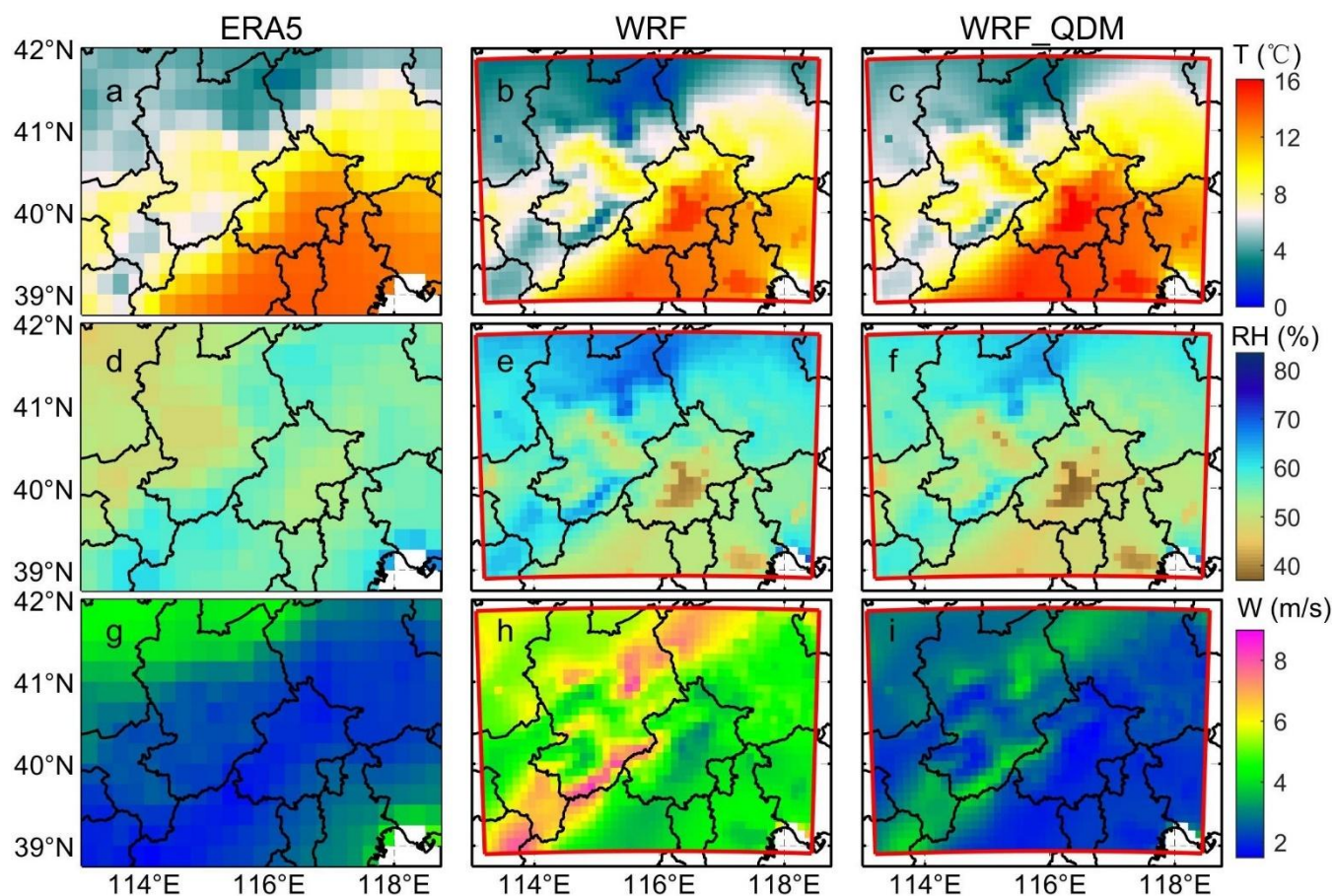




**Figure 6.** The spatial distribution of mean 2 m temperature (a-c), relative humidity (d-f) and 10 m wind speed (g-i) from ERA5, WRF-ESM and WRF-QDM-ESM multi-model ensemble mean during 2008-2017. Figs. S4-S6 shows the four ESM results separately.

285 We use QDM to correct biases of the WRF results for the 2008-2017 historical simulation. The temperature, relative humidity and wind speed from ERA5 over Beijing during 2008-2017 (Fig. 6) have a very similar pattern with that during 1980s (Fig. 3). Average temperatures slightly increased over Beijing compared with the 1980s. Average humidities in most places during 2008-2017 are slightly higher than during the 1980s, while in the northwest of Zhangjiakou where temperatures rose fastest, humidity shows a slight decrease (Fig. 3, Fig. 6). Winds in Beijing between these two decades did not  
290 change.

WRF-QDM-ESM simulations of the three variables (Fig. 6) exhibit geographic patterns that are the same as that during the 1980s (Fig. 3). QDM bias correction makes the temperature hotter and the humidity drier especially in high mountains and cities, producing spatial patterns closer to ERA5 (Fig.  
295 6). QDM bias correction greatly improves wind speed results from uncorrected values of 4-5 m s<sup>-1</sup> to 1.5-2.5 m s<sup>-1</sup> across most areas. The mean 2 m temperature of WRF-QDM-HadGEM is hotter than the other three ESMs (16°C in the center of Beijing), while the other three reach only 14°C, which is close to ERA5 (Fig. S4e-4h). WRF-QDM-MIROC and WRF-QDM-MIROC-CHEM are more humid than WRF-QDM-HadGEM2 and WRF-QDM-BNU. The wind speed of WRF-QDM-BNU is a little smaller  
300 than other three ESMs.

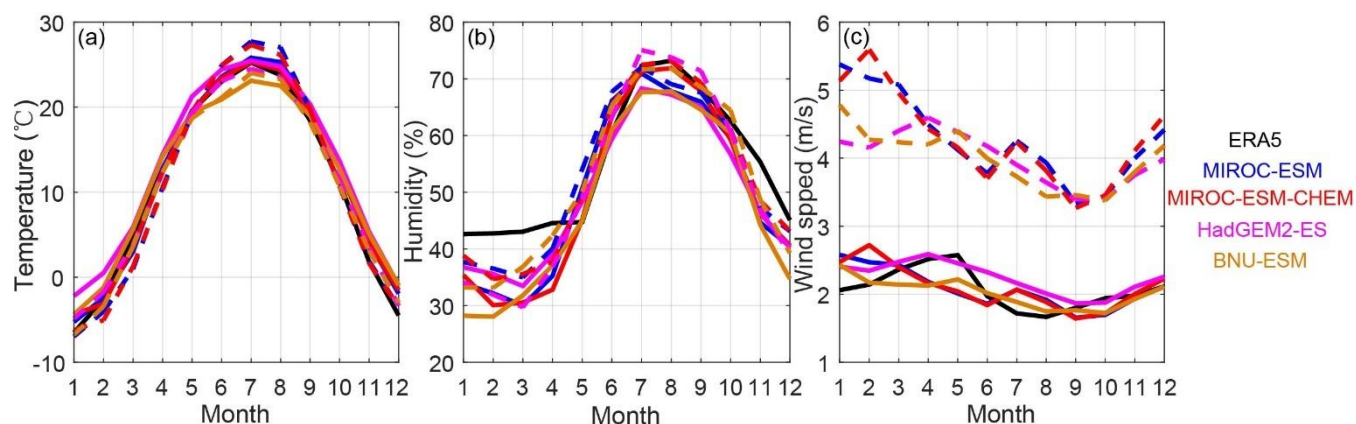
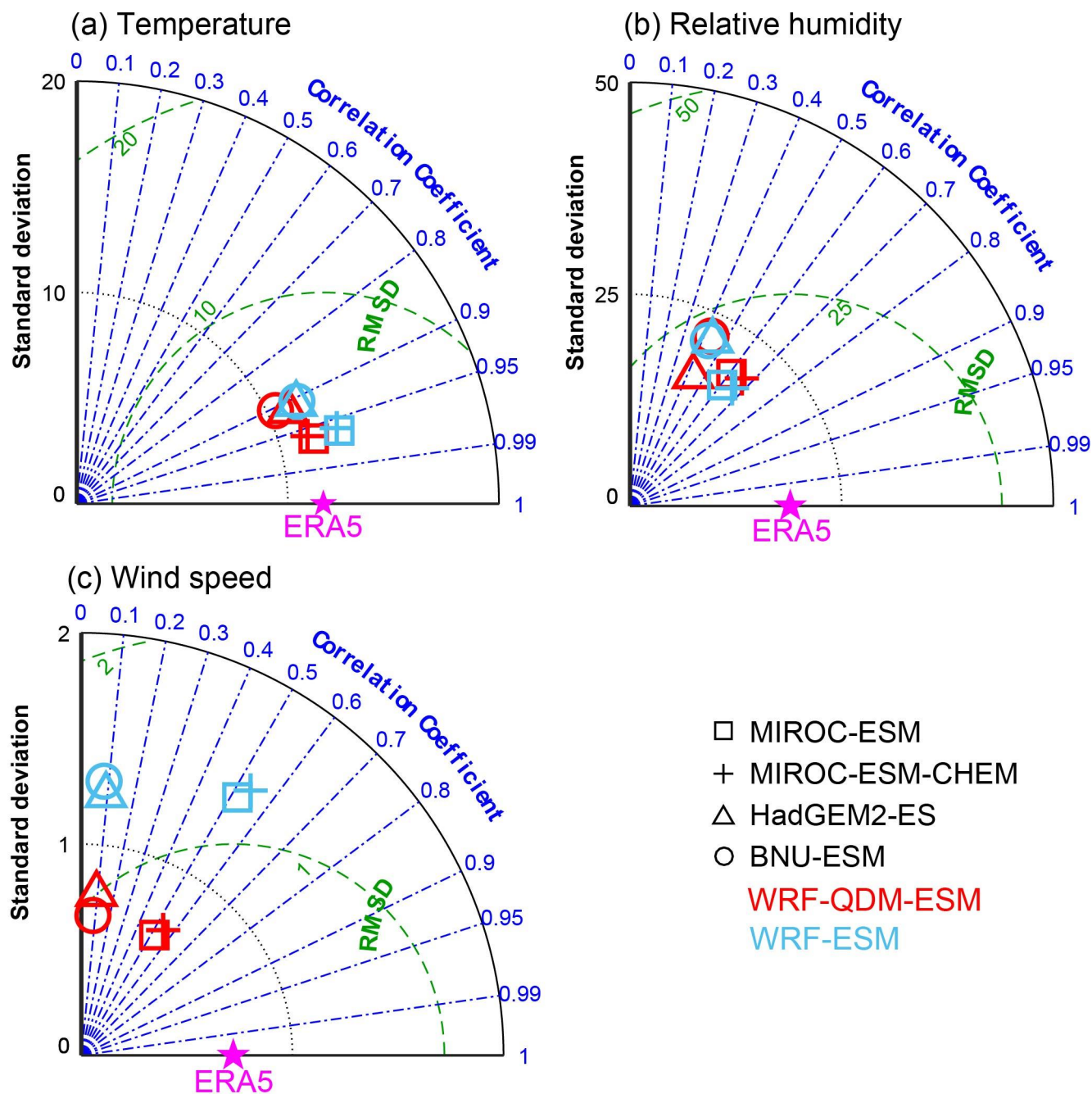




**Figure 7.** Seasonal cycle of multi-year averaged monthly temperature (a), relative humidity (b) and wind speed (c) during 2008-2017 for Beijing. The solid lines are the WRF-QDM-ESM results and the dashed lines are the WRF-ESM results.

305 The seasonal cycle of average daily temperature simulated by WRF is close to ERA5 (Fig. 7). However, the temperature of WRF-QDM-BNU shows a colder bias than the raw results in the summer and the temperature of WRF-QDM-HadGEM2 shows a warmer bias than the results from WRF-HadGEM2 in the winter. For humidity, the overall performances of the WRF-QDM-ESM are not good and they all show a dry bias relative to ERA5 from Jan-May. During Jun-Oct, the humidity from both WRF-QDM-  
310 MIROC and WRF-QDM-MIROC-CHEM show a wetter pattern than ERA5. After bias correction, the wind speed from all ESMs clearly decreased to the same range as ERA5. Winds from HadGEM2-ES shows the best agreement in both the quantity and seasonality with ERA5 but QDM does not change the seasonality of wind speed, just its amplitude.





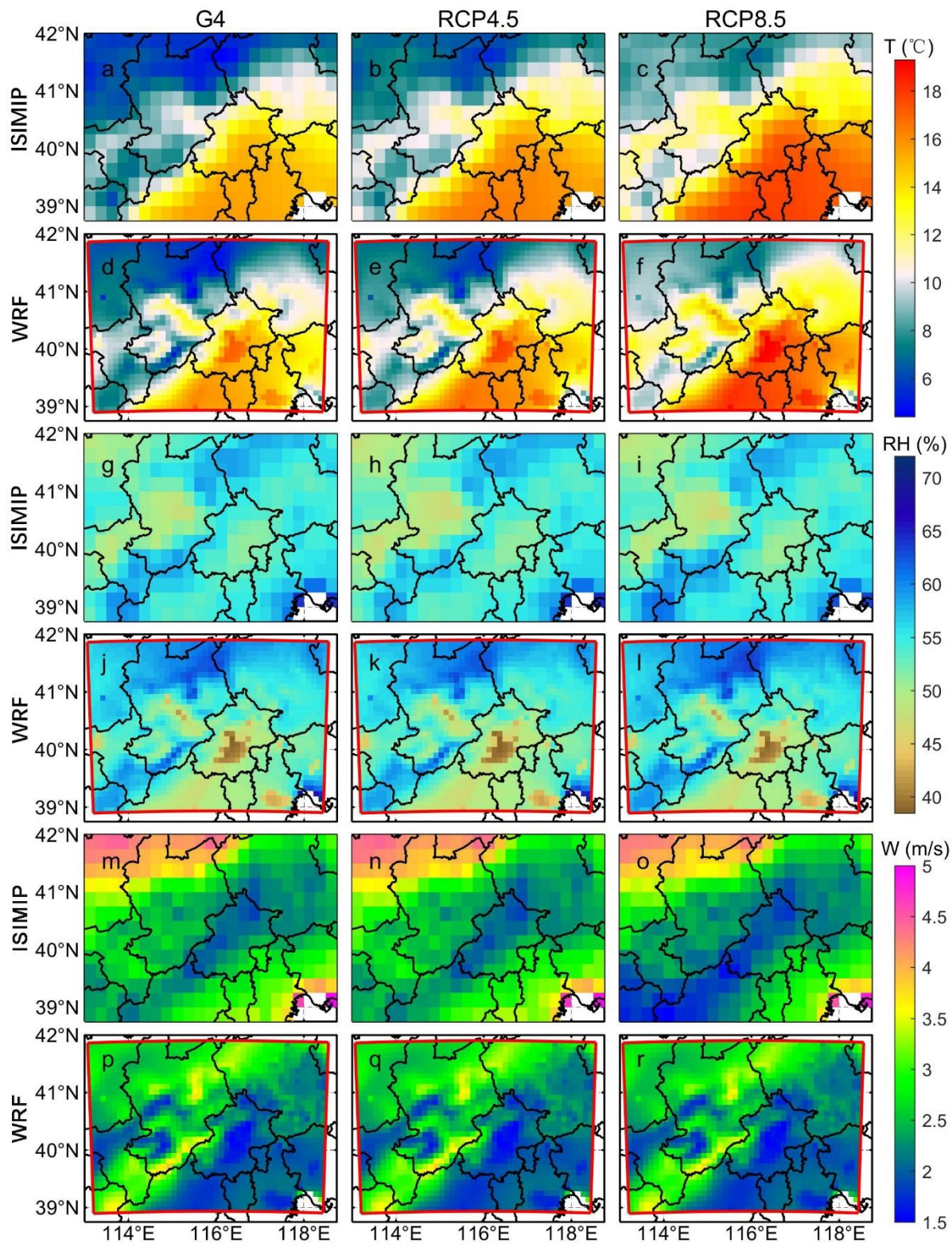
315 **Figure 8.** Taylor diagram for daily temperature (a), relative humidity (b) and wind speed (c) of WRF driven by four ESMs results with QDM bias correction (red) and without bias correction (blue) compared to ERA5 reanalysis data (purple star) during 2008-2017 in Beijing.



The skill of QDM for correcting daily temperature, relative humidity and wind from the biased WRF-ESM are shown in figure 8. QDM changes the errors but has little effect on the correlation with the ERA5 data. While temperature and wind speed all improve with QDM, humidities from WRF-QDM-ESM has a lower performance than does the corresponding WRF-ESM results except for WRF-QDM-HadGEM2. We regard bias correcting as necessary for WRF outputs.

### 3.2 Future Projections

We now look at temperature, humidity and wind projections for 2060-2069. Fig. 9 shows maps of ensemble mean 2 m temperature (Fig. 9a-f), relative humidity (Fig. 9g-l) and 10 m wind speed (Fig. 9m-r) under the G4, RCP4.5 and RCP8.5 scenarios. Mean temperatures over the domain are 12.5 °C, 13.3 °C and 14.8 °C from ISIMIP-ESM, and 13.1 °C, 13.8 °C and 15.2 °C from WRF-QDM-ESM under G4, RCP4.5 and RCP8.5 scenarios respectively. The higher city center temperatures from WRF-QDM-ESM account for the 0.5°C difference from ISIMIP-ESM. Both ISIMIP-ESM and WRF-QDM-ESM produce similar overall temperature patterns driven by topography. Relative humidities under geoengineering and RCP scenarios are almost the same. Mean model relative humidities are 53.8%, 53.6% and 53.4% by ISIMIP-ESM, and slightly wetter than 50.0%, 49.7% and 50.2% from WRF-QDM-ESM, under G4, RCP4.5 and RCP8.5 scenarios respectively. This is mainly due to lower humidities with WRF-QDM-ESM in city centers. Wind spatial patterns are clearly different from ISIMIP-ESM and WRF-QDM-ESM. The windspeed in the southwest and southeast of the domain from ISIMIP-ESM is low, while WRF-QDM-ESM winds are lowest in the city center. Although there are some differences in details between different ESM, the overall results are similar as those of ensemble means (Figs. S7-S12).





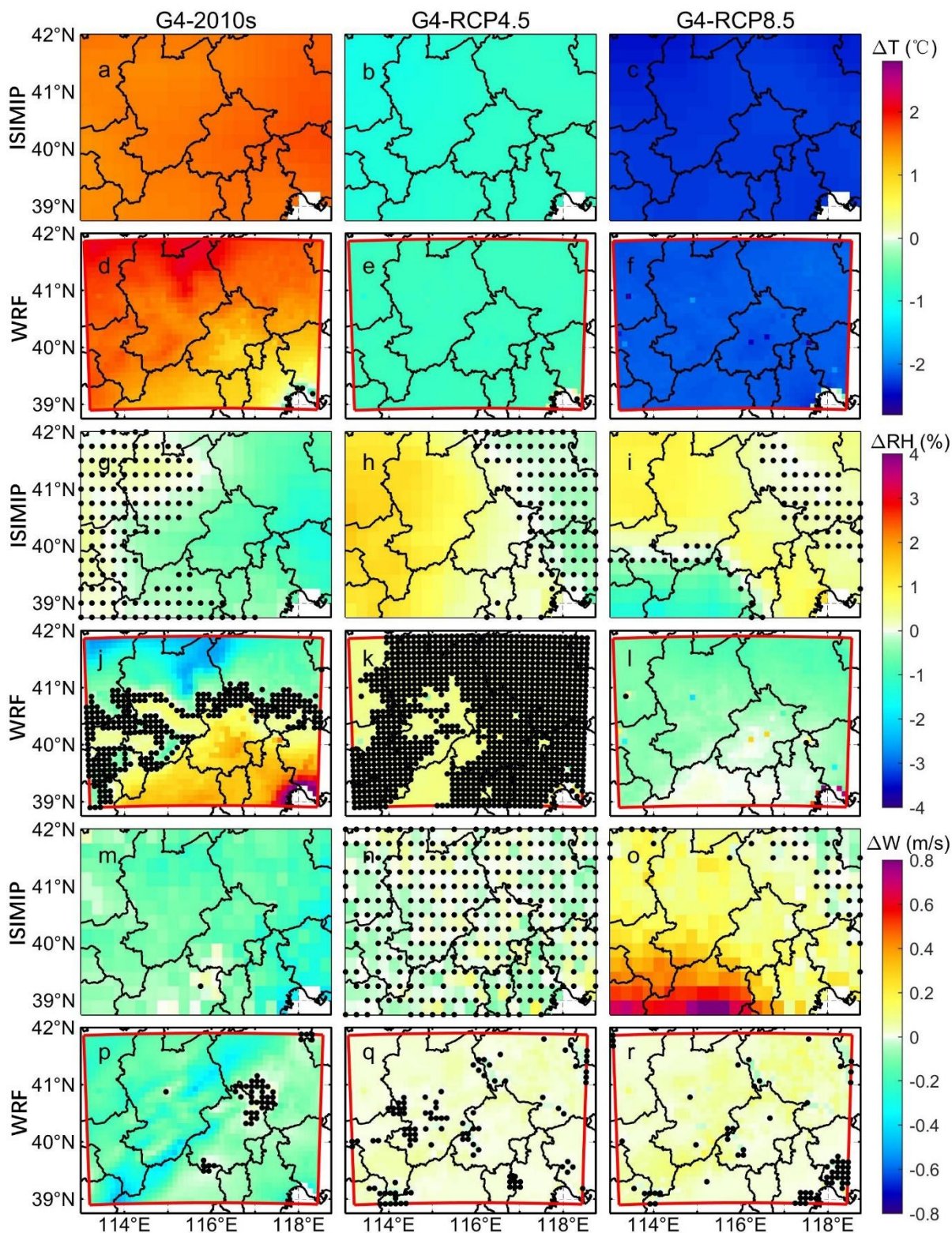
340 **Figure 9.** The spatial distribution of ensemble mean 2 m temperature (a-f), relative humidity (g-l) and  
10 m wind speed (m-r) under G4, RCP4.5 and RCP8.5 scenarios based on ISIMIP-ESM and WRF-  
QDM-ESM results during 2060-2069.

Fig. 10 shows temperature, humidity and wind anomalies from WRF-QDM-ESM and ISIMIP-ESM  
simulations. The mean temperature in the 2060s under G4 is 1-2 °C higher than that during 2008-2017.  
345 Temperatures from both ISIMIP-ESM and WRF-QDM-ESM are cooler over the whole domain under  
G4 than that under RCP4.5 by 0.1~1.5 °C, while there is a larger cooling effect of 1.6~2.8 °C under G4  
relative to RCP8.5 (Table 3). There is large across-model spread with the two MIROC models having  
smaller differences (G4-RCP4.5) than the other two models (Table 3), and the two MIROC models  
show larger differences from each other with ISIMIP-ESM than with WRF-QDM-ESM. Relative  
350 humidity anomalies exhibit large differences under different scenarios for ISIMIP-ESM and WRF-  
QDM-ESM. G4 humidity from ISIMIP-ESM shows a slight reduction of 1 percentage point relative to  
the 2010s over Beijing, while there is an increment of similar magnitude from the WRF-QDM-ESM  
results. When compared to RCP4.5 scenario, the humidity under G4 from ISIMIP-ESM shows a slight  
(1 percentage point) increase, but that from WRF-QDM-ESM shows no statistically significant change.  
355 The differences of relative humidities from WRF-QDM-ESM and ISIMIP-ESM between G4 and  
RCP8.5 show opposite trends although differences are slight. ISIMIP-ESM winds under G4 are a little  
smaller than that during 2010s and show no significant difference between G4 and RCP4.5. Compared  
to RCP8.5, G4 winds from ISIMIP-ESM increase by 0.15 m s<sup>-1</sup> mainly in the south of the domain.  
Winds from WRF-QDM-ESM show very small changes with slight increases relative to the RCP  
360 scenarios. Humidity and windspeed anomalies from ISIMIP appear somewhat spatially anti-correlated,  
while for WRF there are no particular patterns.



365 **Table 3.** Difference of 2 m temperature between G4 and ERA5 in the 2010s and RCP scenarios in the 2060s for the high resolution domain (Fig. 1). Bold indicates the differences or changes are significant at the 95% confidence level according to the Wilcoxon signed rank test. (Units: °C)

	G4-2010s		G4-RCP4.5		G4-RCP8.5	
	ISIMIP	WRF	ISIMIP	WRF	ISIMIP	WRF
MIROC-ESM	<b>1.9</b>	<b>2.0</b>	<b>-0.9</b>	-0.4	<b>-2.3</b>	<b>-1.9</b>
MIROC-ESM-CHEM	<b>2.4</b>	<b>2.0</b>	-0.1	-0.4	<b>-1.6</b>	<b>-1.7</b>
HadGEM2-ES	<b>1.0</b>	<b>0.8</b>	<b>-1.4</b>	<b>-1.5</b>	<b>-2.8</b>	<b>-2.7</b>
BNU-ESM	<b>1.1</b>	<b>1.0</b>	<b>-1.2</b>	<b>-0.7</b>	<b>-2.6</b>	<b>-2.2</b>
Ensemble	<b>1.6</b>	<b>1.5</b>	<b>-0.9</b>	<b>-0.7</b>	<b>-2.3</b>	<b>-2.2</b>





370 **Figure 10.** Spatial pattern of ensemble mean 2 m temperature (a-f), relative humidity (g-l) and 10 m  
wind (m-r) scenario differences: G4-2010s (left column), G4-RCP4.5 (middle column) and G4-RCP8.5  
(right column) based on ISIMIP-ESM and WRF-QDM-ESM results. 2010s means the results simulated  
during 2008-2017, and G4, RCP4.5 and RCP8.5 means the results projected during 2060-2069.  
Stippling indicates grid points where differences are not significant at the 95% confidence level  
according to the Wilcoxon signed rank test. Figs. S13-18 show the results for each ISIMIP-ESM and  
375 WRF-QDM-ESM separately.

#### 4 Discussion and Conclusions

We have explored the impact of geoengineering on surface temperature, humidity and windspeed over  
Beijing during 2060-2069 using statistical bias-correction and dynamical downscaling. We evaluated  
the performance of ISIMIP and WRF methods during 1980-1989 based on the historical simulations  
380 from four ESMs. WRF output needs to be bias-corrected for it to be comparable with observations or  
with statistically downscaled and bias-corrected output. We use the QDM method to correct the bias in  
WRF results since QDM ensures that the pdf of simulation results is consistent with the reanalysis data.  
Because we want to keep the high spatial resolution of the WRF model simulation, we do not correct  
biases grid cell by grid cell, which would produce output at the reanalysis resolution, but instead doing  
385 bias correction for daily mean temperature, humidity and wind speed over the domain.

The raw output from the ESM of temperature, humidity and wind speed, have no clear spatial  
distribution over the domain because cities occupy only a few ESM grid cells. Statistical bias correction  
and downscaling by the ISIMIP method produces output at the same resolution as the observational  
390 reanalysis data and matches its spatial distribution. The ISIMIP method is designed to preserve trends  
and the long-term mean value the same as observations (Hempel et al., 2013). Dynamically  
downscaling demands a higher resolution grid, and WRF produces an output at a spatial resolution  
independent of the resolution of the reanalysis data. WRF results not only produce characteristics  
consistent with the reanalysis data, but also depict the more detailed meteorological characteristics  
395 created by the complex underlying land surface that are input to WRF. The WRF simulation during  
1980-1989 showed higher temperatures in the city centers than that in the suburbs and lower  
temperatures in western and northern mountainous areas. This pattern is created by the joint action of



latitude, terrain and underlying surface. The pattern of relative humidity distribution is anticorrelated to temperature, with lower humidity in the urban center, while humidities in some mountainous areas are  
400 higher. This is similar to the pattern of humidity from 42 AWS in Beijing during 2007-2015 (Yang et al.,  
2017), and due mainly to the underlying surface, and the transpiration of the urban area being less than  
that of the suburbs (Dou et al., 2020). Windspeeds inside the Beijing urban area are low but reach a  
maximum in its western foothills. Urbanization increases surface roughness, lowering windspeed (Liu  
et al., 2020). The pdf of temperature suggests that the WRF result is more realistic and closer to  
405 observations than results from ISIMIP, although the MIROC-ESM and MIROC-ESM-CHEM show a  
higher probability for high temperatures. The pdf of humidity strongly indicates that WRF performs  
better than ISIMIP. But WRF tends to overestimate the wind speed even though the shape of pdf is  
more similar to observations than that of ISIMIP output. Many studies show that WRF frequently  
overestimate the wind speed, e.g., in the Gulf of Mexico (Lee et al., 2011), in the coastal cities of Spain  
410 (Chen et al., 2012), and in south-eastern Texas (Ngan et al., 2013) because of imperfect surface  
representation (e.g., urban vegetation and surface morphology). Overall, for temperature and humidity,  
the results of WRF are better than those of ISIMIP, and both are better than the original ESM output.  
WRF has better correlation with observations than ISIMIP.

415 Applying QDM bias correction to WRF reduces model and monthly dependent differences.  
Temperatures, both before and after bias correction, have high correlations with ERA5 and QDM makes  
little difference. WRF relative humidity, however, is always wetter than that of ERA5 in winter whether  
revised or not. Wind speeds are lowered after bias correction to the same levels as ERA5, but QDM  
does not have a clear effect on correlation (Zhao et al., 2017).

420 The spatial distribution of temperature, humidity and wind speed are roughly similar in all three periods  
assessed, that is the 1980s, 2010s and 2060s, whether from ISIMIP-ESM or WRF-QDM-ESM. Our  
analysis shows that mean temperature under G4 SAI is always lower than that under RCP4.5 and  
RCP8.5. Although it does not return temperatures to the historical level, that was not the design of the  
experiments which instead simply explore the effects of injecting roughly  $\frac{1}{4}$  the amount of  $\text{SO}_2$  into the





425 equatorial lower stratosphere as the 1991 Mt. Pinatubo eruption every year for 50 years. Using ISIMIP  
downscaling leads to larger differences between scenarios than using WRF. HadGEM2-ES shows the  
largest difference in temperatures between G4 and RCP scenarios of the four ESM we study. For the  
relative humidity, ISIMIP-ESM and WRF-QDM-ESM give opposite (but small) signed anomalies  
between G4 and RCP4.5 in our domain. The 2010s were slightly less humid according to WRF-QDM-  
430 ESM than G4 in the 2060s while they were a little wetter according to ISIMIP-ESM.

This paper is the first to use WRF for regional dynamic downscaling of geoengineered climates and  
impacts on relatively small spatial and temporal scales that can be useful for regions that need higher  
resolutions than ERA5 and statistical downscaling can supply. The differences between statistical  
downscaling and dynamic downscaling in the Beijing provincial region, that extends from sea level to  
435 mountains about 2000 m in elevation, may appear rather modest. But even these modest differences in  
derived temperatures and humidities can make for large differences in compound indices such as  
apparent temperature, particularly when assessing future risk to urban populations.

### **Code and data availability**

All ESM data used in this work are available from the Earth System Grid Federation (WCRP, 2021;  
440 <https://esgf-node.llnl.gov/projects/cmip6>, last access: 14 July 2021). The WRF and ISIMIP bias-  
corrected and downscaled results are available for the authors on request. WRF and ISIMIP codes are  
freely available at the references cited in the methods sections.

### **Supplement link**

the link to the supplement will be included by Copernicus.

### **445 Author contribution**

JCM and LZ designed the experiments, JW performed the simulations. JW and JCM prepared the  
manuscript with contributions from all co-authors.



## Competing interests

The authors declare that they have no conflict of interest.

## 450 Disclaimer

Publisher's note: Copernicus Publications remains neutral with regard to jurisdictional claims in published maps and institutional affiliations.

## Special issue statement:

This article is part of the special issue “Resolving uncertainties in solar geoengineering through multi-  
455 model and large-ensemble simulations (ACP/ESD inter-journal SI)”. It is not associated with a conference.

## Acknowledgements

We thank the climate modeling groups for participating in the Geoengineering Model Intercomparison Project and their model development teams; the CLIVAR/WCRP Working Group on Coupled  
460 Modeling for endorsing the GeoMIP; and the scientists managing the earth system grid data nodes who have assisted with making GeoMIP output available. Ben Kravitz provided useful advice on the manuscript. This research was funded by the National Key Science Program for Global Change Research (2015CB953602)

## References

465 Aswathy, V. N., Boucher, O., Quaas, M., Niemeier, U., Muri, H., Mülmenstädt, J., and Quaas, J.: Climate extremes in multi-model simulations of stratospheric aerosol and marine cloud brightening climate engineering, *Atmos. Chem. Phys.*, 15, 9593–9610, <https://doi.org/10.5194/acp-15-9593-2015>, 2015.



- 470 Bao, J., Feng, J., and Wang, Y.: Dynamical downscaling simulation and future projection of  
precipitation over China, *J. Geophys. Res.-Atmos.*, 120(16), 8227-8243,  
<https://doi.org/10.1002/2015JD023275>, 2015.
- Brewer, M. C., and Mass, C. F.: Projected Changes in Heat Extremes and Associated Synoptic- and  
Mesoscale Conditions over the Northwest United States, *J. Climate* 29, 17, 6383-6400,  
<https://doi.org/10.1175/JCLI-D-15-0641.1>, 2016.
- 475 Chen, F., and Dudhia, J.: Coupling an Advanced Land Surface–Hydrology Model with the Penn State–  
NCAR MM5 Modeling System. Part I: Model Implementation and Sensitivity, *Mon. Weather  
Rev.* 129, 4, 569-585, [https://doi.org/10.1175/1520-0493\(2001\)129<0569:CAALSH>2.0.CO;2](https://doi.org/10.1175/1520-0493(2001)129<0569:CAALSH>2.0.CO;2),  
2001.
- Chen, B., Stein, A. F., Castell, N., de la Rosa, J. D., de la Campa, A. M., S., Gonzalez-Castanedo, Y.,  
480 and Draxler, R. R.: Modeling and surface observations of arsenic dispersion from a large Cu-smelter  
in southwestern Europe, *Atmos. Environ.*, 49, 114–122,  
<https://doi.org/10.1016/j.atmosenv.2011.12.014>, 2012.
- Collins, W. J., Bellouin, N., Doutriaux-Boucher, M., Gedney, N., Halloran, P., Hinton, T., Hughes, J.,  
Jones, C. D., Joshi, M., Liddicoat, S., Martin, G., O'Connor, F., Rae, J., Senior, C., Sitch, S.,  
485 Totterdell, I., Wiltshire, A., and Woodward, S.: Development and evaluation of an Earth-System  
model – HadGEM2, *Geosci. Model Dev.*, 4, 1051–1075, <https://doi.org/10.5194/gmd-4-1051-2011>,  
2011.
- Curry, C. L., Sillmann, J., Bronaugh, D., Alterskjaer, K., Cole, J. N. S., Ji, D., Kravitz, B., Kristjánsson,  
J. E., Moore, J. C., Muri, H., Niemeier, U., Robock, A., Tilmes, S., and Yang, S.: A multi-model  
490 examination of climate extremes in an idealized geoengineering experiment, *J. Geophys. Res.-  
Atmos.*, 119, 3900–3923, <https://doi.org/10.1002/2013JD020648>, 2014.
- Dou, J., Bornstein, R., Miao, S., and Zhang, Y.: Observation and Simulation of a Bifurcating  
Thunderstorm over Beijing, *J. Appl. Meteorol. Climatol.*, 59, 2129-2148,  
<https://doi.org/10.1175/JAMC-D-20-0056.1>, 2020.
- 495 Eyring, V.; Gillett, N. P.; Achuta Rao, K. M.; Barimalala, R.; Barimalala Parrillo, M.; Bellouin, N.;  
Cassou, C.; Durack, P. J.; Kosaka, Y.; McGregor, S.; Min, S.; Morgenstern, O.; Ying, S. Human



- Influence on the Climate System. In *Climate Change 2021: The Physical Science Basis. Contribution of Working Group I to the Sixth Assessment Report of the Intergovernmental Panel on Climate Change*, 2nd ed.; Masson-Delmotte, V., Zhai, P., Pirani, A., Connors, S. L., Péan, C., Berger, S., Caud, N., Chen, Y., Goldfarb, L., Gomis, M. I., Huang, M., Leitzell, K., Lonnoy, E., Matthews, J. B. R., Maycock, T. K., Waterfield, T., Yelekçi, O., Yu, R. and Zhou, B., eds.; Cambridge University Press, UK, In Press, 2021.
- 500
- Hempel, S., Frieler, K., Warszawski, L., Schewe, J., and Piontek, F.: A trend-preserving bias correction – the ISI-MIP approach, *Earth Syst. Dynam.*, 4, 219–236, <https://doi.org/10.5194/esd-4-219-2013>,  
505 2013.
- Hersbach, H., Bell, B., Berrisford, P., Biavati, G., Horányi, A., Muñoz Sabater, J., Nicolas, J., Peubey, C., Radu, R., Rozum, I., Schepers, D., Simmons, A., Soci, C., Dee, D., Thépaut, J-N.: ERA5 hourly data on pressure levels from 1979 to present, Copernicus Climate Change Service (C3S) Climate Data Store (CDS), <https://doi.org/10.24381/cds.bd0915c6>, 2018.
- 510 Hong, S. Y., and Lim, J. O. J.: The WRF single-moment 6-class microphysics scheme (WSM6), *J. Korean Meteor. Soc.*, 42(2), 129-151, 2006.
- Iacono, M. J., Delamere, J. S., Mlawer, E. J., Shephard, M. W., Clough, S. A., and Collins, W. D.: Radiative forcing by long-lived greenhouse gases: Calculations with the AER radiative transfer models. *J. Geophys. Res.- Atmos.*, 113(D13), <https://doi.org/10.1029/2008JD009944>, 2008.
- 515 Ji, D., Fang, S., Curry, C. L., Kashimura, H., Watanabe, S., Cole, J. N. S., Lenton, A., Muri, H., Kravitz, B., and Moore, J. C.: Extreme temperature and precipitation response to solar dimming and stratospheric aerosol geoengineering, *Atmos. Chem. Phys.*, 18, 10133–10156, <https://doi.org/10.5194/acp-18-10133-2018>, 2018.
- Ji, D., Wang, L., Feng, J., Wu, Q., Cheng, H., Zhang, Q., Yang, J., Dong, W., Dai, Y., Gong, D., Zhang,  
520 R.-H., Wang, X., Liu, J., Moore, J. C., Chen, D., and Zhou, M.: Description and basic evaluation of Beijing Normal University Earth System Model (BNU-ESM) version 1, *Geosci. Model Dev.*, 7, 2039–2064, <https://doi.org/10.5194/gmd-7-2039-2014>, 2014.



- Jones, A. C., Hawcroft, M. K., Haywood, J. M., Jones, A., Guo, X., and Moore, J. C.: Regional climate impacts of stabilizing global warming at 1.5 K using solar geoengineering, *Earth. Fut.*, 6(2), 230-251, 525 <https://doi.org/10.1002/2017EF000720>, 2018.
- Kain, J. S.: The Kain–Fritsch convective parameterization: an update, *J. Appl. Meteorol.*, 43(1), 170-181, [https://doi.org/10.1175/1520-0450\(2004\)043<0170:TKCPAU>2.0.CO;2](https://doi.org/10.1175/1520-0450(2004)043<0170:TKCPAU>2.0.CO;2), 2004.
- Kawase, H., Yoshikane, T., Hara, M., Kimura, F., Yasunari, T., Ailikun, B., Ueda, H., and Inoue, T.: Intermodel variability of future changes in the Baiu rainband estimated by the pseudo global 530 warming downscaling method, *J. Geophys. Res.-Atmos.*, 114(D24), <https://doi.org/10.1029/2009JD011803>, 2009.
- Kim, D. H., Shin, H. J., and Chung, I. U.: Geoengineering: Impact of marine cloud brightening control on the extreme temperature change over East Asia, *Atmos.*, 11(12), 1345, <https://doi.org/10.3390/atmos11121345>, 2020.
- 535 Kong, X., Wang, A., Bi, X., and Wang, D.: Assessment of temperature extremes in China using RegCM4 and WRF, *Advan. Atmos. Sci.*, 36(4), 363-377, <https://doi.org/10.1007/s00376-018-8144-0>, 2019.
- Kravitz, B., Robock, A., Boucher, O., Schmidt, H., Taylor, K. E., Stenchikov, G., and Schulz, M.: The geoengineering model intercomparison project (GeoMIP), *Atmos. Sci. Lett.*, 12(2), 162-540 167, <https://doi.org/10.1002/asl.316>, 2011.
- Kravitz, B., Robock, A., Tilmes, S., Boucher, O., English, J.M., Irvine, P.J., Jones, A., Lawrence, M.G., MacCracken, M., Muri, H., Moore, J. C., Niemeier, U., Phipps, S.J., Sillmann, J., Storelvmo, T., Wang, H., Watanabe, S.: The Geoengineering Model Intercomparison Project Phase 6 (GeoMIP6): Simulation Design and Preliminary Results, *Geoscientific Model Development* 8, 3379–3392, 545 [doi:10.5194/gmd-8-3379-2015](https://doi.org/10.5194/gmd-8-3379-2015), 2015.
- Kuswanto, H., Kravitz, B., Miftahurrohman, B., Fauzi, F., Sopahaluwaken, A., and Moore, J. C.: Impact of solar geoengineering on temperatures over the Indonesian Maritime Continent, *Int. J. Climatol.*, 1-20, <https://doi.org/10.1002/joc.7391>, 2021.
- Lee, S.-H., Kim, S.-W., Angevine, W. M., Bianco, L., McKeen, S. A., Senff, C. J., Trainer, M., Tucker, 550 S. C., and Zamora, R. J.: Evaluation of urban surface parameterizations in the WRF model using



- measurements during the Texas Air Quality Study 2006 field campaign, *Atmos. Chem. Phys.*, 11, 2127–2143, <https://doi.org/10.5194/acp-11-2127-2011>, 2011.
- Lenton, T. M. and Vaughan, N. E.: The radiative forcing potential of different climate geoengineering options, *Atmos. Chem. Phys.*, 9, 5539–5561, <https://doi.org/10.5194/acp-9-5539-2009>, 2009.
- 555 Li, X., and Babovic, V.: Multi-site multivariate downscaling of global climate model outputs: an integrated framework combining quantile mapping, stochastic weather generator and Empirical Copula approaches, *Clim. Dyn.*, 52, 5775–5799, <https://doi.org/10.1007/s00382-018-4480-0>, 2019.
- Liu, Y., Xu, Y., Zhang, F., and Shu, W.: A preliminary study on the influence of Beijing urban spatial morphology on near-surface wind speed, *Urban Clim.*, 34, 100703, 560 <https://doi.org/10.1016/j.uclim.2020.100703>, 2020.
- MacMartin, D. G., and Kravitz, B.: Multi-model dynamic climate emulator for solar geoengineering, *Atmos. Chem. Phys. Discuss.*, p. in review, <https://doi.org/10.5194/acp-2016-535>, 10, 2016.
- McSweeney, C. F., and Jones, R. G.: How representative is the spread of climate projections from the 565 CMIP5 GCMs used in ISI-MIP?, *Clim. Services*, 1, 24–29, <https://doi.org/10.1016/j.cliser.2016.02.001>, 2016.
- Meng, X. G., Guo, J. J., and Han, Y. Q.: Preliminary assessment of ERA5 reanalysis data, *J. Mar. Meteor.*, 38, 91–99, <https://doi.org/10.19513/j.cnki.issn2096-3599.2018.01.011>, 2018. (in Chinese)
- Michalakes, J., Chen, S., Dudhia, J., Hart, L., Klemp, J., Middlecoff, J., and Skamarock, 570 W.: Development of a next-generation regional weather research and forecast model, *Developments in Teracomputing*, W. Zwiefelhofer and N. Kreitz, Eds., World Scientific, 269–296, 2001.
- Moore, J. C., Yue, C., Zhao, L., Guo, X., Watanabe, S., and Ji, D.: Greenland ice sheet response to stratospheric aerosol injection geoengineering, *Earth's Future*, 7(12), 1451–1463, <https://doi.org/10.1029/2019EF001393>, 2019.
- 575 Ngan, F., Kim, H., Lee, P., Al-Wali, K., and Dornblaser, B.: A study of nocturnal surface wind speed overprediction by the WRF-ARW model in southeastern Texas, *J. Appl. Meteor.*, 52(12), 2638–2653, <https://doi.org/10.1175/JAMC-D-13-060.1>, 2013.



- Niemeier, U. and Timmreck, C.: What is the limit of climate engineering by stratospheric injection of SO<sub>2</sub>?, *Atmos. Chem. Phys.*, 15, 9129–9141, <https://doi.org/10.5194/acp-15-9129-2015>, 2015.
- 580 Noh, Y., Cheon, W. G., Hong, S. Y., and Raasch, S.: Improvement of the K-profile model for the planetary boundary layer based on large eddy simulation data, *Boundary-layer meteorology*, 107(2), 401-427, <https://doi.org/10.1023/A:1022146015946>, 2003.
- Pachauri, R. K. , Allen, M. R. , Barros, V. R. , Broome, J. , Cramer, W. , Christ, R. , Church, J. A. , Clarke, L. , Dahe, Q. , Dasgupta, P. , Dubash, N. K. , Edenhofer, O. , Elgizouli, I. , Field, C. B. , Forster, P. , Friedlingstein, P. , Fuglestvedt, J. , Gomez-Echeverri, L. , Hallegatte, S. , Hegerl, G. , Howden, M. , Jiang, K. , Jimenez Cisneroz, B. , Kattsov, V. , Lee, H. , Mach, K. J. , Marotzke, J. , Mastrandrea, M. D. , Meyer, L. , Minx, J. , Mulugetta, Y. , O'Brien, K. , Oppenheimer, M. , Pereira, J. J. , Pichs-Madruga, R. , Plattner, G. K. , Pörtner, H. O. , Power, S. B. , Preston, B. , Ravindranath, N. H. , Reisinger, A. , Riahi, K. , Rusticucci, M. , Scholes, R. , Seyboth, K. , Sokona, Y. , Stavins, R. , Stocker, T. F. , Tschakert, P. , van Vuuren, D. and van Ypserle, J. P.:  
590 Climate Change 2014: Synthesis Report. Contribution of Working Groups I, II and III to the Fifth Assessment Report of the Intergovernmental Panel on Climate Change / R. Pachauri and L. Meyer (editors), Geneva, Switzerland, IPCC, 151 p., ISBN: 978-92-9169-143-2, 2014.
- Paulson, C. A.: The mathematical representation of wind speed and temperature profiles in the unstable  
595 atmospheric surface layer, *J. Appl. Meteorol.*, 9(6), 857-861, [https://doi.org/10.1175/1520-0450\(1970\)009<0857:TMROWS>2.0.CO;2](https://doi.org/10.1175/1520-0450(1970)009<0857:TMROWS>2.0.CO;2), 1970.
- Pielke Sr, R. A.: *Climate vulnerability: understanding and addressing threats to essential resources*, Elsevier, 2013.
- Riahi, K., Rao, S., Krey, V., Cho, C., Chirkov, V., Fischer, G., Kindermann, G., Nakicenovic, N., and  
600 Rafaj, P.: RCP 8.5—A scenario of comparatively high greenhouse gas emissions, *Clim. chang.*, 109(1), 33-57, <https://doi.org/10.1007/s10584-011-0149-y>, 2011.
- Robock, A., Marquardt, A., Kravitz, B., and Stenchikov, G.: Benefits, risks, and costs of stratospheric geoengineering, *Geophys. Res. Lett.*, 36(19), <https://doi.org/10.1029/2009GL039209>, 2009.



- Salvi, K., Kannan, S., and Ghosh, S.: Statistical downscaling and bias-correction for projections of  
605 Indian rainfall and temperature in climate change studies, In 4th International Conference on  
Environmental and Computer Science (Vol. 19, pp. 16-18), 2011.
- Schmidt, H., Alterskjær, K., Bou Karam, D., Boucher, O., Jones, A., Kristjánsson, J. E., Niemeier, U.,  
Schulz, M., Aaheim, A., Benduhn, F., Lawrence, M., and Timmreck, C.: Solar irradiance reduction  
to counteract radiative forcing from a quadrupling of CO<sub>2</sub>: climate responses simulated by four  
610 earth system models, *Earth Syst. Dynam.*, 3, 63–78, <https://doi.org/10.5194/esd-3-63-2012>, 2012.
- Schoof, J. T., Pryor, S. C., and Ford, T. W.: Projected changes in united states regional extreme heat  
days derived from bivariate quantile mapping of cmip5 simulations, *J. Geophys. Res.-Atmos.*,  
124(10), 5214-5232, <https://doi.org/10.1029/2018JD029599>, 2019.
- Shepherd, J.: Geoengineering the climate: Science, governance, and uncertainty, Royal Society Policy  
615 document 10/09, 82 pp, 2009.
- Taylor K. E.: Summarizing multiple aspects of model performance in a single diagram, *J. Geophys.  
Res.-Atmos.*, 106(D7), 7183-7192, 2001.
- Thomson, A. M., Calvin, K. V., Smith, S. J., Kyle, G. P., Volke, A., Patel, P., Delgado-Arias, S., Bond-  
Lamberty, B., Wise, M. A., Clarke, L. E., and Edmonds, J. A.: RCP4.5: a pathway for stabilization  
620 of radiative forcing by 2100, *Climatic Change*, 109, 77, <https://doi.org/10.1007/s10584-011-0151-4>,  
2011.
- Tilmes, S., Fasullo, J., Lamarque, J.F., Marsh, D.R., Mills, M., Alterskjaer, K., Muri, H., Kristjánsson,  
J.E., Boucher, O., Schulz, M., Cole, J.N.S., Curry, C.L., Jones, A., Haywood, J., Irvine, P.J., Ji, D.,  
Moore, J. C., Karam, D.B., Kravitz, B., Rasch, P.J., Singh, B., Yoon, J. H., Niemeier, U., Schmidt,  
625 H., Robock, A., Yang, S. and Watanabe, S.: The hydrological impact of geoengineering in the  
Geoengineering Model Intercomparison Project (GeoMIP), *J. Geophys. Res.- Atmos.*, 118, 11036-  
11058, <https://doi.org/10.1002/jgrd.50868>, 2013.
- Vandyck, T., Keramidas, K., Saveyn, B., Kitous, A., and Vrontisi, Z.: A global stocktake of the Paris  
pledges: implications for energy systems and economy, *Global environmental change*, 41, 46-63,  
630 <https://doi.org/10.1016/j.gloenvcha.2016.08.006>, 2016.





- Wang, J., Feng, J., Yan, Z., Hu, Y., and Jia, G.: Nested high-resolution modeling of the impact of urbanization on regional climate in three vast urban agglomerations in China, *J. Geophys. Res.-Atmos.*, 117(D21), <https://doi.org/10.1029/2012JD018226>, 2012.
- 635 Watanabe, S., Hajima, T., Sudo, K., Nagashima, T., Takemura, T., Okajima, H., Nozawa, T., Kawase, H., Abe, M., Yokohata, T., Ise, T., Sato, H., Kato, E., Takata, K., Emori, S., and Kawamiya, M.: MIROC-ESM 2010: model description and basic results of CMIP5-20c3m experiments, *Geosci. Model Dev.*, 4, 845–872, <https://doi.org/10.5194/gmd-4-845-2011>, 2011.
- Wilby, R. L., and Dawson, C. W.: Using SDSM version 3.1—A decision support tool for the assessment of regional climate change impacts, *User manual*, 8, 2004.
- 640 Wilcke, R. A. I., Mendlik, T., and Gobiet, A.: Multi-variable error correction of regional climate models, *Clim. chang.*, 120(4), 871-887, <https://doi.org/10.1007/s10584-013-0845-x>, 2013.
- Xu, Z., and Yang, Z. L.: An improved dynamical downscaling method with GCM bias corrections and its validation with 30 years of climate simulations, *J. Clim.*, 25(18), 6271-6286, <https://doi.org/10.1175/JCLI-D-12-00005.1>, 2012.
- 645 Yang, P., Ren, G., and Hou, W.: Temporal–spatial patterns of relative humidity and the urban dryness island effect in Beijing City, *J. Appl. Meteorol.*, 56(8), 2221-2237, <https://doi.org/10.1175/JAMC-D-16-0338.1>, 2017.
- Zhao, T., Bennett, J. C., Wang, Q. J., Schepen, A., Wood, A. W., Robertson, D. E., and Ramos, M. H.: How suitable is quantile mapping for postprocessing GCM precipitation forecasts?, *J. Clim.*, 30(9), 650 3185-3196, <https://doi.org/10.1175/JCLI-D-16-0652.1>, 2017.